EAI Endorsed Transactions
on Energy Web Research Article **EAI.EU**

Research on Land-Based Wind/Solar Power Station Site Deformation Monitoring Based on SBAS-InSAR Technology

Junke Guo[1], Ling Liu[1,*], Yongfeng Zheng[1], Wei Cai[1], Zhijun Wang[1], Shangqi Wang[1]

[1] Zhejiang Electric Power Design Institute Co., Ltd, China Energy Engineering Group, Hangzhou, Zhejiang Province, China, 310000

Abstract

INTRODUCTION: In recent years, China has been building extensive wind/solar power stations. During the construction and operation of land-based wind/solar power stations, deformation monitoring is an important method to investigate the station stability.
OBJECTIVES: Therefore, this study uses Sentinel-1 data and time-series InSAR technology to monitor the deformation of photovoltaic and wind power stations in Qingyuan County.
METHODS: InSAR technology obtains deformation rate maps in the radar line of sight (LOS) direction for a wide area around the power station sites. Since wind/solar power stations are mainly located in natural environments with relatively dense vegetation coverage, this paper proposes a SBAS-InSAR method integrated with spatiotemporal filtering to accurately extract the time series deformation over a large area. Based on the statistical characteristic difference between the deformation and the atmospheric delay, spatiotemporal filterings are applied to remove the atmospheric delay from the InSAR derived deformation results.
RESULTS: The experimental results show that spatiotemporal filtering is an effective and fast method to remove atmospheric delay.
CONCLUSION: The integration of BSAS-InSAR with spatiotemporal filtering has great potential applications in the deformation monitoring of land-based wind/solar power station sites, which is critical for the construction and operation of land-based wind/solar power stations.

Keywords: Land-based Wind/Solar Power Station; Deformation Monitoring; Time Series; SBAS-InSAR

Received on 26 December 2023, accepted on 29 March 2024, published on 05 April 2024

doi: 10.4108/ew.5656

1. Introduction

Wind power and photovoltaic energy have emerged as one of the most promising new energy sources, and in recent years China has been building extensive land-based wind/solar power stations [1]. During the operation and construction of a wind/solar power station, the station stability is affected by a number of factors. On the one hand, geologic hazards (e.g., landslide, collapse and surface subsidence) around the wind/solar power station may pose a threat to wind turbine and photovoltaic panel. On the other hand, the construction and operation of a power station also changes the stability of surrounding environment, and the health of the power station infrastructure needs to be monitored over time. Therefore, deformation monitoring is important for the operation and construction of land-based wind/solar power stations.

Conventional deformation monitoring of mountain wind/solar power stations is currently focused on ground-based measurements such as levelling, GPS measurements, short-range photogrammetry, and distributed fiber sensors [2,3]. However, these inefficient and costly methods are insufficient for long-term deformation monitoring of wind/solar power stations. Differential Synthetic aperture

---

[*] Corresponding author. Email: 598334204@qq.com

radar interferometry (D-InSAR) technology developed at the end of the 20th century shows tremendous advantages in earth observation. It can accurately extract minute surface deformation information from hundreds of kilometers away, with measurement accuracy reaching centimeter to millimeter level [4]. With all-weather observation capability, D-InSAR has the advantages of a large detection range, stable repetition cycle, and high spatial resolution [5,6], theoretically more suitable for long-term, large-area regional deformation monitoring. It has been used in the measurement of surface deformation for hazard investigation [7-9]. However, there have been few studies based on InSAR for wind/solar station deformation monitoring.

The traditional D-InSAR technique can measure surface deformations within two SAR images. However, D-InSAR technology is easily affected by atmospheric delay disturbances and decorrelation, making it difficult to accurately extract deformation information [10,11]. To overcome the aforementioned problems faced by D-InSAR technology, a variety of advanced InSAR methods, utilizing approaches grounded in time series SAR acquisitions, have been proposed by numerous scholars worldwide [12-16]. In 2001, Italian scholar Ferretti publicly introduced the Permanent Scatterer InSAR technique (PS-InSAR) [15], known as the first-generation time series InSAR technology. After the introduction of the PS-InSAR method, some similar PS-InSAR techniques were subsequently developed [16-17]. Although the implementation details of these algorithms differ, their main guiding ideas are essentially consistent. They analyze the temporal phase signals of high coherence point targets extracted from multi-temporal radar datasets to invert the average velocity and surface time series deformation in the study area [18]. Alongside the development of PS-InSAR technology, technology based on Small Baseline Subset (SBAS) utilizing Distributed Scatterers (DS) has been evolved [12,13]. Since DS is susceptible to spatio-temporal decorrelation and coherence is maintained only in interferometric pairs with small spatio-temporal baselines, the traditional single master-baseline combination strategy is no longer applicable. SBAS-InSAR employs multiple master interferograms with short temporal and spatial baselines, enhancing its ability to mitigate decorrelation effects more effectively than PS-InSAR. Therefore, it is better suited for deformation monitoring applications in natural environments.

Atmospheric delay represents a widespread problematic factor in large-scale displacement monitoring using InSAR, particularly in areas characterized by steep topography and moist climates [19,20]. Various approaches are available to estimate and compensate for atmospheric delays. For instance, weather models with regular global availability can be successfully applied to estimate atmospheric delays [21,22]. Empirical relationships between atmospheric phase and elevation can also be used to estimate stratospheric tropospheric delays [23,24]. However, both methods require extensive computations to be performed. Typically, the atmospheric phase term exhibits temporal randomness and spatial coherence, in contrast to the ground deformation signal, which tends to display low frequencies across both temporal and spatial dimensions. Based on the statistical characteristic difference between the deformation and the atmospheric delay, we can use spatiotemporal filtering to rapidly ad remove atmospheric delay. This approach is supposed to improve the accuracy of SBAS-InSAR in the large-region with high efficiency and wide adaptability.

Therefore, this paper focuses on the deformation monitoring of wind/solar power stations located in natural environments with relatively dense vegetation cover. We propose a SBAS-InSAR method integrated with spatiotemporal filtering to accurately extract time series deformations. The time-series InSAR not only opens up a broad spectrum of possibilities for deformation monitoring, leading to significant savings over conventional monitoring methods, but also enables the extraction of historical deformation in key monitoring areas and their monitoring follow-up using historical archival data from radar satellites. It has great potential applications for deformability monitoring of land-based wind/solar power station sites.

2. Study area and SAR Data

Qingyuan County is situated in the southwestern part of Zhejiang Province, occupying the domain 27°25 ' N-27°51' N and 118°50 ' E-119°30' E. The terrain of Qingyuan County belongs to the middle mountainous area of southwest Zhejiang Province, with a variety of landforms, such as valleys, basins, hills, low mountains and middle mountains. The terrain of Qingyuan County is rugged, featuring surface elevations that vary between 240 m and 1860 m.

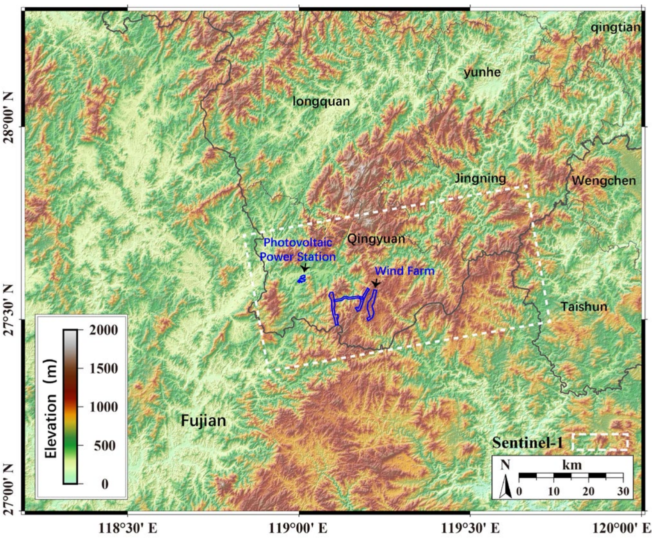

Figure 1. The study area and SAR image coverage

This study primarily uses Sentinel-1A data covering the Qingyuan County area from the past two years. The Sentinel-1 satellite carries a C-band Synthetic Aperture Radar (SAR) sensor and operates in a sun-synchronous, near-polar orbit. The shortest revisit cycle of a single satellite is 12 days, and it has multiple imaging modes, capable of realizing single polarization, dual polarization, and other polarization modes. The Sentinel-1 data are freely accessible, with wide spatial coverage and short revisit periods. Its resolution and wavelength generally meet the requirements of temporal monitoring in mountainous regions, making it suitable for large-scale surface deformation time series analysis in the project area. Figure 1 shows the data coverage of bursts 158-159 in the iw3 swath of Sentinel-1 within the white dashed frame of the project area.

In addition to SAR data, other auxiliary satellite data are also required: (1) DEM data is derived from AW3D30 data, a high-precision global digital surface model (DSM) released for free by the Japan Aerospace Exploration Agency (JAXA) in May 2015. This dataset features a horizontal resolution of 30 meters (1 arc-second) and boasts an elevation accuracy of 5 meters. (2) Optical remote sensing images, utilizing historical image data from Google Earth software released by Google, are used to assist in the interpretation and reading of InSAR results.

3.SAR Data Processing Method

To overcome the shortcomings of D-InSAR, such as atmospheric delays and DEM errors, Ferretti and others proposed PS-InSAR based on high coherence point targets. Nevertheless, in the PS method, as it relies on a single reference master image, the decorrelation phenomenon becomes more pronounced with longer spatio-temporal baselines, particularly in mountainous regions with limited artificial structures. It may even be impossible to obtain enough PS points for reliable monitoring results.

In comparison to PS-InSAR, SBAS-InSAR proves to be effective in mitigating decorrelation effects, making it a preferred choice for measuring the displacement rates of landslides in wind/solar power stations within natural environments. Consequently, the SBAS-InSAR method is primarily employed for time series InSAR processing in this study. It is widely acknowledged that interferograms in natural scenes are susceptible to noise contamination resulting from temporal and spatial decorrelation. By establishing multiple master image pairs, this method restricts the spatio-temporal baselines to a narrower range, thereby minimizing the impact of spatio-temporal decorrelation. The following section provides a summary of the detailed steps involved in the SBAS-InSAR approach.

Assuming $N+1$ images are obtained at times $t_0, t_1, \cdots, t_N$, by setting spatial-temporal baseline thresholds, radar image pairs are constructed, and differential interferometry is performed to obtain M differential interferograms, where M should satisfy:

$$\frac{N+1}{2} \leq M \leq \frac{N(N+1)}{2} \qquad (1)$$

Subsequently, M interferograms are unwrapped. Assuming that all differential interferograms are correctly unwrapped, the sequences of the master and reference images are respectively $[IM_1, \cdots, IM_M]$ and $[IS_1, \cdots, IS_M]$, with the observation time of the reference images lagging behind that of the master images, i.e., $IS_j > IM_j (j = 1, \cdots, M)$. Therefore, the unwrapped phase in the j-th differential interferogram can be represented as:

$$\begin{aligned} \delta\phi_j &= \phi_{ISj} - \phi_{IMj} \\ &\approx \left(\phi_{def}^{t_B} - \phi_{def}^{t_A}\right) + \frac{4\pi}{\lambda}\frac{B_\perp}{R\sin\theta}\Delta h + \phi_{atm}^j \\ &+ \phi_{noi}^j, t_0 \leq t_A < t_B \leq t_N \qquad (2) \end{aligned}$$

Taking the moment t_0 as a reference, t_A and t_B are the imaging times of the master and reference images of the j-th interferogram, respectively. $\phi_{def}^{t_A}$ and $\phi_{def}^{t_B}$ are the LOS (Line of Sight) deformation phases relative to the initial moment t_0 at times t_A and t_B, respectively; Δh is the DEM (Digital Elevation Model) elevation error at that point, with the phase caused by this error related to the and incidence angle θ, slant range R, perpendicular baseline $B_\perp$; ϕ_{noi}^j is the noise phase; ϕ_{atm}^j is the atmospheric delay phase.

Assuming the low-frequency phase of surface deformation at any time has a functional relationship with time as follows:

$$\begin{aligned} \phi_{def}(t_i) = \bar{v} \cdot (t_i - t_0) + \frac{1}{2}\bar{a} \cdot (t_i - t_0)^2 + \frac{1}{6}\triangle \bar{a} \\ \cdot (t_i - t_0)^3, i = 0,1, \cdots, N \qquad (3) \end{aligned}$$

where $\bar{v}$, $\bar{a}$, and $\triangle \bar{a}$ are three unknown parameters, representing the average velocity, average acceleration, and rate of change of average acceleration in the LOS direction; therefore, Equation (4) can be expanded as:

$$\begin{aligned} \delta\phi_j = \bar{v} \cdot (t_B - t_A) + \frac{1}{2}\bar{a} \cdot [(t_B - t_0)^2 - (t_A - t_0)^2] + \frac{1}{6} \\ \triangle \bar{a} \cdot [(t_B - t_0)^3 - (t_A - t_0)^3] \\ + \frac{4\pi}{\lambda}\frac{B_{\perp j}}{R\sin\theta}\Delta h + \phi_{res}^j \qquad (4) \end{aligned}$$

where, $\Delta\phi_{res}^j$is the sum of the noise phase, atmospheric delay phase, and residual deformation phase; the above equation can be rewritten in matrix form as:

$$\delta\phi = AP = [BF, c]\begin{bmatrix} p^T \\ \Delta h \end{bmatrix} \qquad (5)$$

p is the parameter of the Surface Deformation Model$[\bar{v}, \bar{a}, \triangle \bar{a}]$; c is the coefficient matrix of elevation error Δ , $c = [(4\pi/\lambda)(B_{\perp 1}/R\sin\theta), \cdots, (4\pi/\lambda)(B_{\perp M}/R\sin\theta)]^T$; B is an M×N matrix, where the elements of the matrix $B[i,j] = t_j - t_{j-1}(IM_i \leq j \leq IS_i - 1, i = 1, \cdots, M)$, and all other elements are zero; F is an $N \times 3$ coefficient matrix, whose values are:

$$F = \begin{bmatrix} 1 & \frac{t_1 - t_0}{2} & \frac{(t_1 - t_0)^2}{6} \\ 1 & \frac{t_2 + t_1 - 2t_0}{2} & \frac{(t_2 - t_0)^3 - (t_1 - t_0)^3}{6(t_2 - t_0)} \\ \cdots & \cdots & \cdots \\ 1 & \frac{t_N + t_{N-1} - 2t_0}{2} & \frac{(t_N - t_0)^3 - (t_{N-1} - t_0)^3}{6(t_N - t_{N-1})} \end{bmatrix} \qquad (6)$$

When $M \geq 4$, the least squares method can be used to solve for the optimal solution of the four unknown parameters:

$$\hat{P} = (A^T A)^{-1} A^T \delta\phi \qquad (7)$$

After calculating the deformation model parameters ($\bar{v}$, $\bar{a}$, $\triangle \bar{a}$) and elevation error Δh, we substitute them back into Equation (4) to extract the residual phase term $\Delta\phi_{res}$. Filter based on the spatiotemporal characteristics differences among the noise phase, atmospheric delay phase, and residual deformation phase: The deformation phase is correlated both spatially and temporally; the atmospheric delay phase is correlated spatially but not temporally; the noise phase manifests as a high-frequency signal in both spatial and temporal domains, whereas the atmospheric delay phase can be extracted by employing spatial low-pass and temporal high-pass filtering techniques.

After removing the DEM error and atmospheric delay, the unwrapped phase only contains the deformation phase and noise phase:

$$\begin{aligned}\delta\phi_j{}' &= \delta\phi_j - \Delta\phi_{topo}^j - \phi_{atm}^j \\ &\approx \left(\phi_{def}^{t_B} - \phi_{def}^{t_A}\right) + \phi_{noi}^j \qquad (8)\end{aligned}$$

Assuming that the deformation rate is linear between two adjacent time intervals, that is, the deformation is piecewise linear over the entire observation period, the above equation can be rewritten in matrix form as:

$$\delta\phi' = Bv \qquad (9)$$

where v is the piecewise linear deformation rate to be determined $[v_1, v_2, \cdots, v_N]$, B is an $M \times N$ coefficient matrix, with matrix elements $B[i,j] = t_j - t_{j-1} (IM_i \leq j \leq IS_i - 1, i = 1, \cdots, M)$, and all other elements are zero. When all interferograms are in the same subset, matrix B is invertible, and the deformation rate can be directly solved using the least squares method. However, when there are $L (L > 1)$ discontinuous interferogram subsets due to the limitation of baseline length, matrix B is rank-deficient. Singular Value Decomposition (SVD) can be applied to matrix B to obtain the generalized inverse solution for the final deformation rate. By integrating the deformation rate of each time period over time, the deformation time series for the entire observation period can be obtained.

As noted above, atmospheric delays pose significant challenges for large-area deformation measurement using InSAR, particularly in areas characterized by humid climates and steep terrain [19,20]. Typically, the signal related to surface deformation displays low frequencies in both spatial and temporal domain, whereas the atmospheric phase exhibits spatial autocorrelation and temporal decorrelation [25]. As a result, it is possible to separate the atmospheric delay from the deformation signal using their statistical characteristics. In this paper, a combination of temporal and spatial filters is employed to achieve this separation. Initially, a linear least-squares temporal filter is utilized to estimate the temporally uncorrelated components of the time series deformation. Subsequently, a quadratic weighted average spatial filter is applied to further separate the spatially autocorrelated and temporally uncorrelated components. Consequently, the resulting terms primarily encompassing atmospheric delay can be effectively separated.

4. InSAR Monitoring Results and Analysis for Wind/Solar Power Stations in Qingyuan County

4.1. InSAR Preprocessing Results and Analysis

Before the time-series InSAR processing, the interferometric preprocessing of the SAR data is first performed. The main steps include SAR image stitching, image registration and resampling, differential interferometry, and filtering. Due to the unique TOPS imaging mode of the Sentinel-1 data, it was necessary to stitch the burst data and then register it [26]. Based on the project area, bursts 158-159 from the iw3 swath of Sentinel-1 data were selected for stitching. The stitched Sentinel-1 amplitude map and the coverage area of the photovoltaic power station and wind farm are shown in Figure 2. Due to the unique TOPS imaging mode of Sentinel-1, its registration accuracy must reach 0.001 pixels. Otherwise, there will be a jump between the two bursts, leading to an error in the interferometric results. The Sentinel-1 image from 2022 January 18 was applied as the master image, and the remaining 61 images were registered using this master image as a reference.

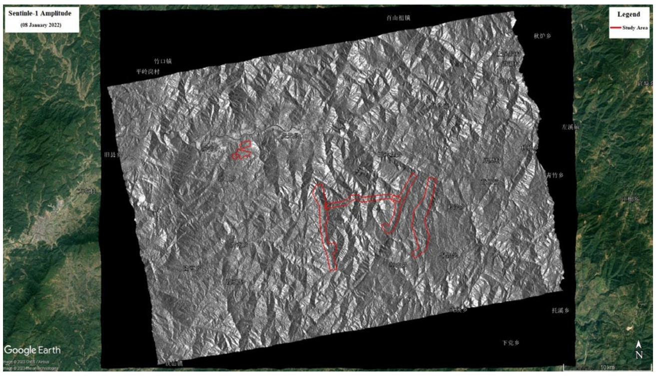

Figure 2. Sentinel-1 Amplitude Image (08 January 2022) and Regional Coverage Area

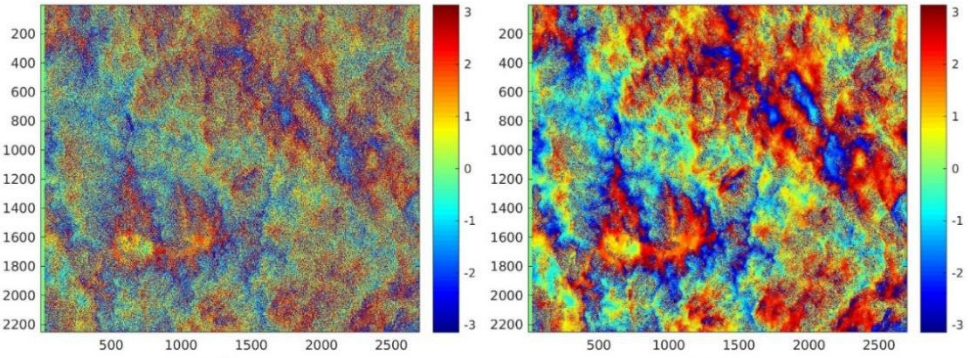

Figure 3. Differential Interferogram of Sentinel-1 Images (20230218 VS. 20230314); (a) Original Phase; (b) Phase After Filtering

After accurately registering the SAR images, the next step is differential interferometry. Considering the spatial sampling rate of Sentinel-1 image data is 2.3m×13.9m (range direction × azimuth direction), the subsequent differential interferometry processing adopts a multilook parameter of 5:1. Differential interferometry involves conjugate multiplication of complex images of the master and slave scenarios to obtain an interferometric phase map and calculate the path difference of the two radar beams. Taking the SAR images from 18 February 2023 and 14 March 2023, as examples, with the former as the master image, the differential interferometric phase obtained is shown in Figure 3(a). It can be seen that there are certain phase changes in different areas, and there are also obvious noise signals in the phase map.

Since the original differential interferometric phase is severely affected by noise, it is necessary to filter the interferogram before proceeding with time series processing. Adaptive filtering is performed using a filtering function based on the local fringe spectrum. Figure 3(b) shows the interferometric phase map after filtering. It is clear that the filtering operation significantly reduces the noise in the interferogram, making the interference fringes sharper. Furthermore, coherence is another important quantitative measure of the quality of an interferogram, where higher coherence values indicate better quality. Figure 4 shows a plot of the coherence distribution of the interferogram before and after filtering. It can be seen that before filtering, most regions in the natural scene have low coherence, with the exception of some regions in urban areas, and the interferogram is greatly affected by noise. After filtering, the coherence is significantly improved in most regions. This demonstrates that the filtering operation greatly enhances the quality of the interferogram, which is beneficial for subsequent time series InSAR analysis and processing.

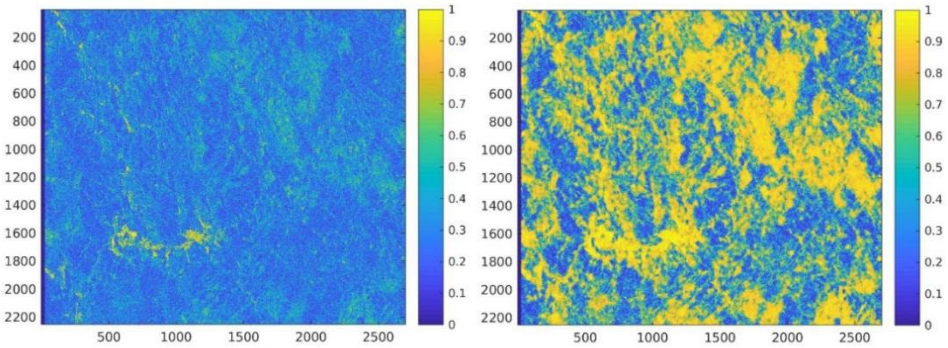

Figure 4. Coherence Distribution Map (20230218 VS. 20230314); (a) Coherence Before Filtering; (b) Coherence After Filtering

4.2. Time Series InSAR Processing Results and Analysis of the Surrounding Area

In SBAS-InSAR processing, it is first necessary to set appropriate spatio-temporal baseline thresholds. Considering the regional vegetation coverage and the characteristics of the

C-band Sentinel-1 data, a strategy with a maximum spatial baseline of 300 m was adopted to ensure that each image formed an interferometric pair with the two following images. The 62 Sentinel-1 images thus form 121 interferometric pairs, and the spatial-temporal baseline combinations of the corresponding image pairs are shown in Figure 5.

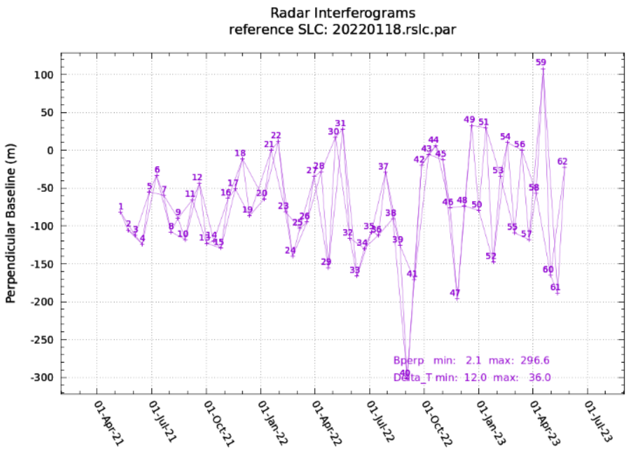

Figure 5. Sentinel-1 Image Interferometric Pair Combinations and Spatio-Temporal Baseline Distribution

Based on the above image pair combination strategy, around 1.05 million effective measurement points are obtained in a region of aabout 1450 km² around the photovoltaic power station and wind farm. As mentioned earlier, the presence of atmospheric delay poses as a widespread nuisance factor when it comes to estimating large-area displacements using InSAR. Figure 6 shows the statistical distribution of the monitoring results derived from the basic SBAS-InSAR method and the proposed SBAS-InSAR integrated with spatiotemporal filtering. Compared to the basic SBAS-InSAR method, the proposed SBAS-InSAR results are mainly concentrated around zero. The statistical results show that the basic SBAS-InSAR results have a standard deviation (Std) of 25.8 mm/year and a mean of -0.1 mm/year, while the results of the proposed SBAS-InSAR integrated with spatiotemporal filtering have a Std of 9.6 mm/year and a mean of -0.4 mm/year. It indicates that the proposed SBAS-InSAR method has higher accuracy, and achieves improvement about 62.8% than the basic SBAS-InSAR method.

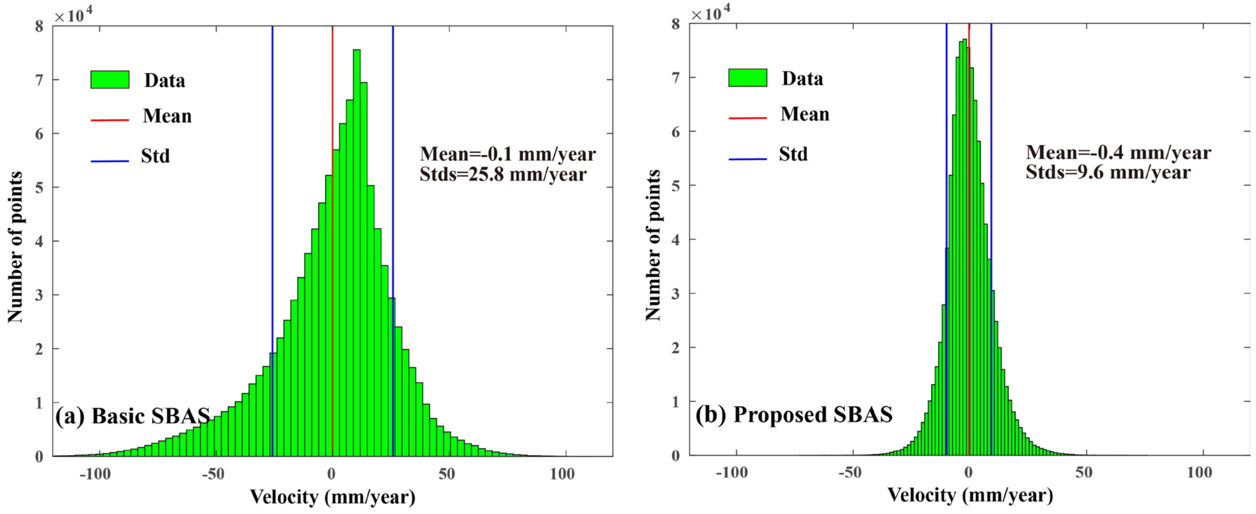

Figure 6. Statistical Distribution Map of Average Annual Deformation Rate in LOS Direction in the Monitored Region; (a) the basic SBAS-InSAR method; (b) the proposed SBAS-InSAR integrated with spatiotemporal filtering

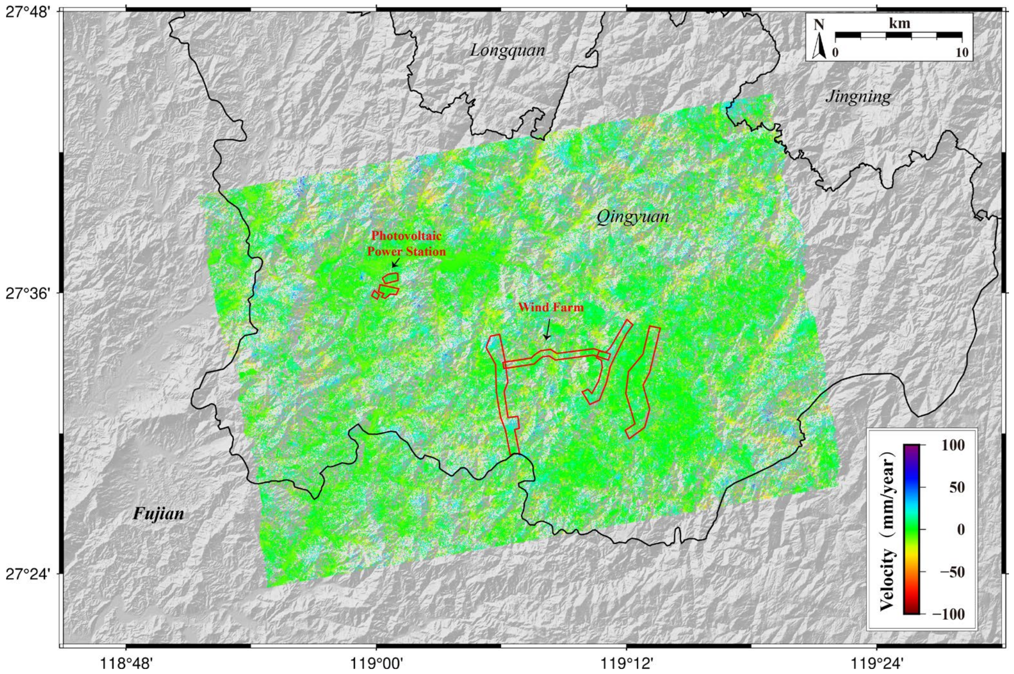

Figure 7. Distribution Map of Annual Average LOS Deformation Velocity in the Monitoring Area

4.3. The analysis of the InSAR results for the photovoltaic power station

Figure 8 presents the distribution of the LOS mean annual deformation rate in the photovoltaic region together with the optical images. The time-series InSAR analysis was performed from May 2021 to May 2023, while the optical images were acquired in February 2023. Based on the InSAR results, it can be observed that all three blocks of the PV area remained stable during the monitoring period, showing no significant signs of deformation photovoltaic. The only deformed area in the monitoring region (G4 area in Figure 8a) is located to the west of the photovoltaic area. Corresponding optical imagery revealed the location to be a construction site in an urban area with exposed bare ground. It has been tentatively inferred that this localized ground deformation is caused by construction activity. This result also indirectly confirms the accuracy of the InSAR monitoring results.

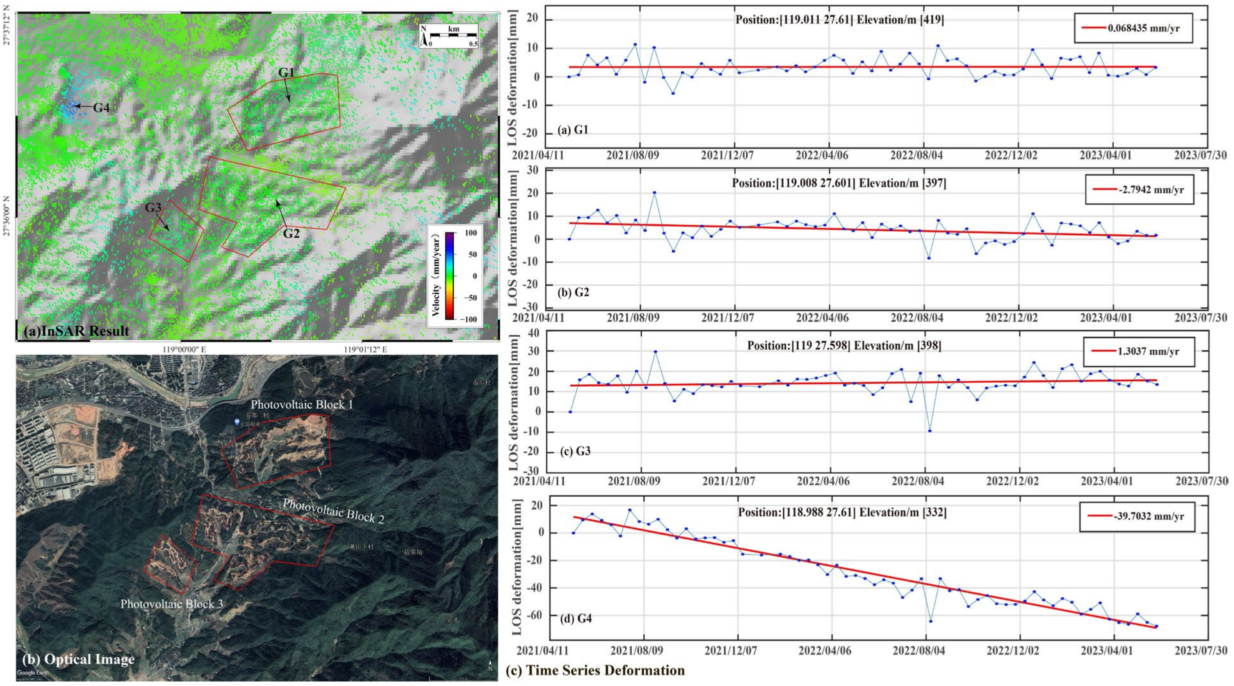

Figure 8. Distribution and optical image of LOS annual mean deformation rate in the photovoltaic region; (a) LOS deformation rate; (b) Optical images from February 2023; (c) Deformation diagram of G1-G4 point time series

Further, one point was selected from each of the three photovoltaic blocks and the western construction area (labeled as G1-G4 in Figure 8a) to illustrate the time series deformation obtained from InSAR monitoring. Based on the time series deformation, it can be observed that the deformation sequences in the three photovoltaic blocks (i.e., G1, G2, and G3 points) fluctuate around zero, showing no significant deformation over time and remaining in a stable state. In contrast, the G4 point situated in the western part of the photovoltaic area exhibits a nearly linear deformation trend in the time dimension, with a LOS deformation rate of approximately -39.7 mm/year. Based on the previous analysis combined with optical remote sensing imagery, it was inferred that the deformation in this area may be attributed to the natural consolidation of the exposed soil in the construction zone. However, due to its distance, this deformation does not have a significant effect on the photovoltaic area.

4.4. Wind Farm InSAR Results Analysis

Figure 9 shows the distribution of the LOS annual mean deformation rate in the wind farm region together with an optical image. The time-series InSAR analysis spans from May 2021 to May 2023, with optical images acquired in February 2023. Fig. 9 shows that it can be observed that the InSAR monitoring results exhibit more significant noise compared to the photovoltaic region due to the steep terrain and dense vegetation in this region. There is no evidence of large-scale deformation in this region, but there are localized regions of deformation. These are located primarily within the wind farm block one at points F1 and F2. In addition, a slight deformation signal is observed at point F3 outside the project area. The wind farm blocks 1, 3, and 4 appear to be stable and no significant deformation is detected.

Similarly, deformation positions were selected from the monitoring area, and five points (Figure 9a, F1-F5) were chosen to display the time series deformation obtained from InSAR monitoring in this area, as shown in Figure 9c. From the results of the time series analysis, it can be observed that the three main deformation areas in the wind farm area (i.e., points F1, F2, and F3) remained relatively stable during the monitoring period, with no apparent acceleration. Considering the deformation locations from InSAR and optical images, these deformations are primarily located on the mountain slopes, most likely caused by local slope instabilities. Further monitoring during the construction of future wind power facilities and roads may be desirable. On the other hand, the points F4 and F5 in the wind power blocks 2, 3, and 4 remain stable during the monitoring period, while the deformation sequence obtained from the InSAR monitoring fluctuates around zero. The overall area remained stable.

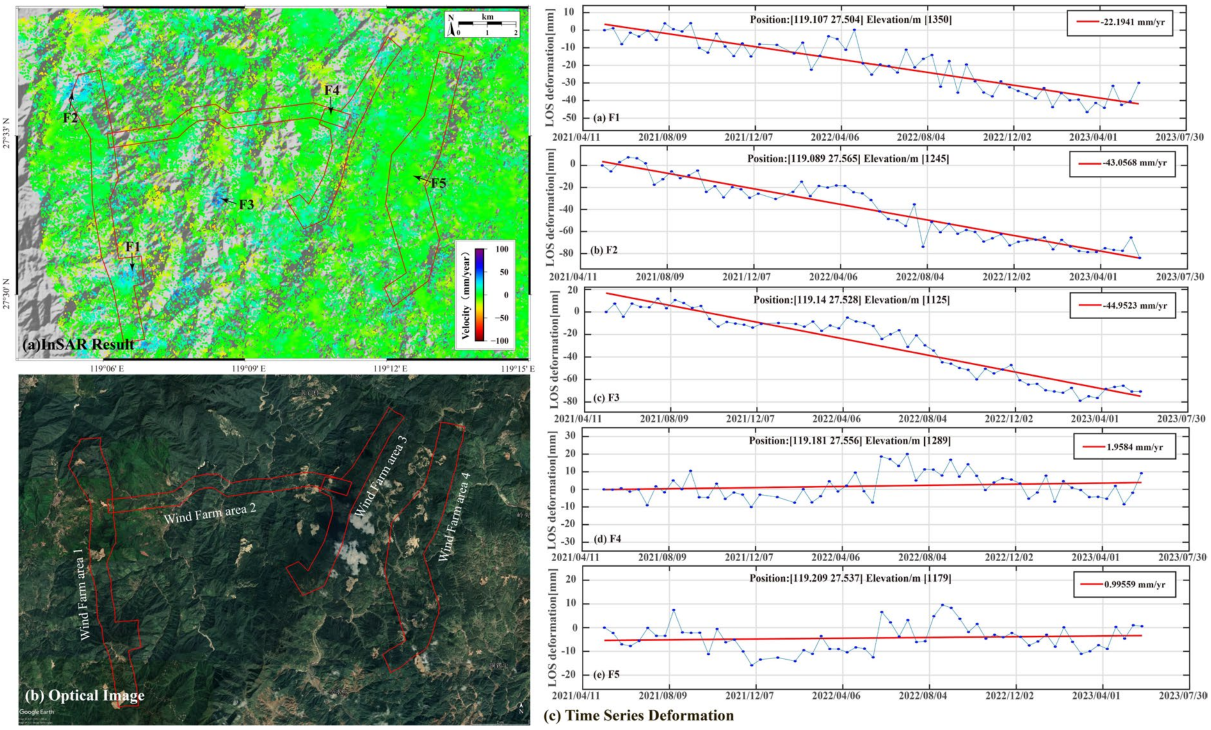
(a)InSAR Result

(b) Optical Image

(c) Time Series Deformation

Figure 9. LOS annual average deformation rate distribution in the wind farm area along with an optical image; (a) LOS deformation rate, (b) optical image from February 2023, and (c) time series deformation plots for points F1 to F5

4. Conclusions

In this paper, we propose an SBAS-InSAR integrated spatiotemporal filtering to process 62 scenes of Sentinel-1 data from May 2021 to May 2023. It obtained surface deformation monitoring results for photovoltaic and wind power stations and their surrounding 1450 km2 area. The results show that the proposed SBAS-InSAR method is more accurate and achieves an improvement of about 62.8 percent over the basic SBAS-InSAR method. In addition, the results showed that there was no sign of large-scale deformation in the monitoring area in Qingyuan County, and the area around the photovoltaic and wind power plants was generally stable. Further detailed analysis of the photovoltaic and wind power areas revealed that the geological conditions around the photovoltaic areas remained stable and showed no signs of deformation during the monitoring period.photovoltaic In Wind Power Block 1, there are two localized deformation regions on the slope, but there is currently no sign of accelerated deformation. There is no sign of deformation and geological conditions are stable in the Wind Power Block 2, 3 and 4. This paper demonstrates that the SBAS-InSAR method is suitable for large-scale potential deformation surveys in wind and solar power stations located in relatively dense natural environments, significantly reducing the cost of conventional monitoring methods.

Acknowledgements.

The research was supported by the Key Technology Research Project for Integrated Intelligent Monitoring of Onshore Wind/Solar Stations, Sky and Ground (Project Number: DG3-L01-2022).

References

[1] Wang, Y., Chao, Q., Zhao, L., & Chang, R.. Assessment of wind and photovoltaic power potential in China. Carbon Neutrality. 2022; 1(1), 15.

[2] Lin, C. K., Dai, C. Y., & Wu, J. C. Analysis of structural deformation and deformation-induced solar radiation misalignment in a tracking photovoltaic system. Renewable energy. 2013; 59, 65-74.

[3] Abdollahi, R. Impact of wind on strength and deformation of solar photovoltaic modules. Environmental Science and Pollution Research. 2021; 28(17), 21589-21598.

[4] Raucoules, D., et al., Validation and intercomparison of Persistent Scatterers Interferometry: PSIC4 project results. Journal of Applied Geophysics, 2009. 68(3): p. 335-347.

[5] Cigna, F., Osmanoglu, B., Cabral-Cano, E.. Dixon, T.H, Avila-Olivera, J.A., Garduno-Monroy, V.H., DeMets, C., Wdowinski, S. Monitoring land subsidence and its induced

geological hazard with synthetic aperture radar interferometry: A case study in Morelia, Mexico. Remote Sens. Environ. 2012;117,146-161.

[6] Costantini, M., Ferretti, A., Minati, F., Falco, S., Trillo, F., Colombo, D., Novali, F..Malvarosa, F., Mammone, C., Vecchioli, F., Rucci, A., Fumagalli, A., Allievi, J..Ciminelli. M.G.. Costabile. S. Analysis of surface deformations over the whole Italian territory by interferometric processing of ERS, Envisat and COSMO-Sky Medradar data. Remote Sens. Environ. 2017; 202,250-275.

[7] Osmanoğlu, B., Sunar, F., Wdowinski, S., Cabral-Cano, E. Time series analysis of InSAR data: Methods and trends. ISPRS J. Photogramm. Remote Sens. 2016; 115, 90-102.

[8] Massonnet, D., Rossi, M., Carmona, C., Adragna, F., Peltzer, G., Feigl, K., Rabaute, T. The displacement field of the Landers earthquake mapped by radar interferometry. Nature. 1993; 364 (6433), 138–142.

[9] Wasowski, J., Bovenga, F. Investigating landslides and unstable slopes with satellite Multi Temporal Interferometry: Current issues and future perspectives. Eng. Geol. 2014; 174, 103-138.

[10] Crosetto, M., Monserrat, O., Bremmer, C., Hanssen, R., Capes, R., Marsh, S.Ground motion monitoring using SAR interferometry: quality assessment. Eur.Geol. 2009; 26, 12–15.

[11] Colesanti, C., & Wasowski, J. Investigating landslides with space-borne Synthetic Aperture Radar (SAR) interferometry. Engineering geology. 2006; 88(3-4), 173-199.

[12] Berardino, P., Costantini, M., Franceschetti, G., Iodice, A., Pietranera, L., & Rizzo, V. Use of differential SAR interferometry in monitoring and modelling large slope instability at Maratea (Basilicata, Italy). Engineering Geology. 2003; 68(1-2), 31-51.

[13] Lanari, R., Mora, O., Manunta, M., Mallorquí, J. J., Berardino, P., & Sansosti, E. A small-baseline approach for investigating deformations on full-resolution differential SAR interferograms. IEEE transactions on geoscience and remote sensing. 2004; 42(7), 1377-1386.

[14] Casu, F., Manzo, M., & Lanari, R. A quantitative assessment of the SBAS algorithm performance for surface deformation retrieval from DInSAR data. Remote Sensing of Environment. 2006; 102(3-4), 195-210.

[15] Ferretti, A., Prati, C., & Rocca, F. Permanent scatterers in SAR interferometry. IEEE Transactions on geoscience and remote sensing. 2001; 39(1), 8-20.

[16] Hooper, A., Zebker, H., Segall, P., & Kampes, B. A new method for measuring deformation on volcanoes and other natural terrains using InSAR persistent scatterers. Geophysical research letters; 2004; 31(23).

[17] Hu, X., Biirgmann, R., Schulz, W.H., Fielding, E.J. Four-dimensional surface motions of the Slumgullion landslide and quantification of hydrometeorological forcing. Nat.Commun. 2020; 11,2792.

[18] Huang, O., Crosetto, M., Monserrat, 0., Crippa, B. Displacement monitoring and modelling of a high-speed railway bridge using C-band Sentinel-1 data. ISPRS J.Photogramm.Remote Sens. 2017; 128204-211.

[19] Liu, X., Zhao, C., Zhang, Q., Lu, Z., Li, Z., Yang, C., ... & Liu, C. Integration of Sentinel-1 and ALOS/PALSAR-2 SAR datasets for mapping active landslides along the Jinsha River corridor, China. Eng. Geol. 2021; 284, 106033.

[20] Li, Z., Muller, J. P., Cross, P., Fielding, E. J. Interferometric synthetic aperture radar (InSAR) atmospheric correction: GPS, Moderate Resolution Imaging Spectroradiometer (MODIS), and InSAR integration. J. Geophys. Res. Solid Earth. 2005; 110(B3).

[21] Doin, M.P., Lasserre, C., Peltzer, G., Cavalié, O., Doubre, C. Corrections of stratified tropospheric delays in SAR interferometry: validation with global atmospheric models. J. Appl. Geophys. 2009; 69, 35–50.

[22] Jolivet, R., Grandin, R., Lasserre, C., Doin, M.P., Peltzer, G. Systematic InSAR tropospheric phase delay corrections from global meteorological reanalysis data. Geophys. Res. Lett. 2011; 38.

[23] Beauducel, F., Briole, P., Froger, J.-L. Volcano-wide fringes in ERS synthetic aperture radar interferograms of Etna (1992–1998): deformation or tropospheric effect? Journal of Geophysical Research: Solid Earth. 2000; 105, 16391–16402.

[24] Dong, J., Zhang, L., Liao, M., & Gong, J. Improved correction of seasonal tropospheric delay in InSAR observations for landslide deformation monitoring. Remote Sensing of Environment. 2019; 233, 111370.

[25] Werner, C., Wegmuller, U., Strozzi, T., Wiesmann, A. Interferometric point target analysis for deformation mapping. Geoscience and Remote Sensing Symposium, 2003. IGARSS'03. Proceedings.

[26] Cai, J., Zhang, L., Dong, J., Guo, J., Wang, Y., & Liao, M. Automatic identification of active landslides over wide areas from time-series InSAR measurements using Faster RCNN. International Journal of Applied Earth Observation and Geoinformation. 2023; 124, 103516.